

Journal of
Applied Remote Sensing

RemoteSensing.SPIEDigitalLibrary.org

Radar high-speed maneuvering target detection based on joint second-order keystone transform and modified integrated cubic phase function

Jiancheng Zhang
Tao Su
Yanyan Li
Jibin Zheng

SPIE.

Jiancheng Zhang, Tao Su, Yanyan Li, Jibin Zheng, "Radar high-speed maneuvering target detection based on joint second-order keystone transform and modified integrated cubic phase function," *J. Appl. Remote Sens.* **10**(3), 035009 (2016), doi: 10.1117/1.JRS.10.035009.

Radar high-speed maneuvering target detection based on joint second-order keystone transform and modified integrated cubic phase function

Jiancheng Zhang,* Tao Su, Yanyan Li, and Jibin Zheng

Xidian University, National Laboratory of Radar Signal Processing, 2 South Taibai Road, Xi'an 710071, China

Abstract. Long-time coherent integration is an effective means to improve the radar detection ability of high-speed maneuvering targets with jerk motion. However, the range migration (RM) and Doppler frequency migration (DFM) have a great impact on the integration performance. To overcome these problems, a unique method, called the second-order keystone transform modified integrated cubic phase function (SKT-MICPF), is proposed. In this method, the velocity compensation and SKT are jointly employed to correct the RM. After the RM correction, the azimuth echoes of a range cell where a target is located can be modeled as a cubic phase signal (CPS), whose chirp rate (CR) and quadratic CR are related to the target's radial acceleration and jerk, respectively. Thereafter, an effective parameters' estimation algorithm for CPS, called MICPF, is proposed and applied to compensate the DFM. After that, coherent integration and target detection are accomplished via the fast Fourier transform and constant false alarm rate technique, successively. Compared with the improved axis rotation discrete chirp Fourier transform, the SKT-MICPF achieves close detection performance, but greatly reduces the computational complexity. The results of simulation and real radar data demonstrate the validity of the proposed algorithm. © The Authors. Published by SPIE under a Creative Commons Attribution 3.0 Unported License. Distribution or reproduction of this work in whole or in part requires full attribution of the original publication, including its DOI. [DOI: [10.1117/1.JRS.10.035009](https://doi.org/10.1117/1.JRS.10.035009)]

Keywords: radar target detection; parameter estimation; cubic phase signal; range migration correction; Doppler frequency migration compensation.

Paper 16177 received Mar. 7, 2016; accepted for publication Jul. 12, 2016; published online Aug. 3, 2016.

1 Introduction

Modern national defenses have higher requirements for the detection of high-speed maneuvering targets.^{1,2} Prolonging the integration time is an effective means to improve the detection performance. However, with the increasing of the integration time, the integration performance will degrade due to the range migration (RM) and Doppler frequency migration (DFM). To address these problems, various successful algorithms¹⁻¹⁵ have been developed.

The Radon Fourier transform (RFT),² the keystone transform (KT),³ the axis rotation moving target detection,⁴ and the scaled inverse Fourier transform-based method⁵ can be applied to correct the RM and accomplish coherent integration for a target with a uniform radial velocity. The Radon fractional FT,⁶ the Radon Lv's distribution (RLVD),⁷ the KT Lv's transform,⁸ the two-dimensional (2-D) match filter-based method,⁹ and the KT-RFT¹⁰ are the effective methods for a high-speed maneuvering target with a uniform radial acceleration. However, for a highly maneuvering target with a jerky motion, the aforementioned algorithms²⁻¹⁰ will suffer from integration loss due to the RM and DFM induced by the target's jerky motion.

For a high-speed maneuvering target with a uniform jerk, an algorithm based on the generalized KT and second-order dechirp process is proposed in Ref. 11, which employs the range frequency domain form of the compressed echoes, i.e., Eq. (5), to accomplish the target's motion parameters estimation. However, because the target's energy spreads in the range frequency

*Address all correspondence to: Jiancheng Zhang, E-mail: zjc7836@126.com

domain, this method suffers from great signal-to-noise ratio (SNR) loss. The cubic phase function (CPF)-based methods^{12,13} and the adjacent correlation function LVT¹⁴ also face similar problems. An improved axis rotation discrete chirp Fourier transform (IAR-DCFT) method is presented in Ref. 15, which can correct the RM by the IAR, and achieve coherent integration via the DCFT. Nevertheless, the implementation of the DCFT is computationally demanding.^{16,17}

After the RM correction, the azimuth echoes of a range cell where a target is located can be considered as a cubic phase signal (CPS), whose chirp rate (CR) and quadratic CR (QCR) are related to the target's radial acceleration and jerk, respectively. Therefore, the estimation algorithms for the CPS can be applied to estimate the target's radial acceleration and jerk to further compensate the DFM. The scaled FT (SCFT)-based method,¹⁸ the keystone time chirp rate distribution,¹⁹ and the modified chirp rate quadratic chirp rate distribution²⁰ are the successful algorithms for CPS. However, due to the fourth-order kernel functions that are applied, the antinoise performances of those methods are still low. The integrated cubic phase function (ICPF)²¹ which is developed from the CPF^{22,23} can obtain a higher antinoise performance than the aforementioned approaches¹⁸⁻²⁰ due to its bilinearity. In Ref. 24, a space switching-based ICPF (SS-ICPF) algorithm is proposed for CPS. Nevertheless, the space switch method which includes the circular shifting operation and map operation would burden the complexity of the estimator and increase the computational cost.

Motivated by the previous work, an algorithm, known as second-order keystone transform modified integrated cubic phase function (SKT-MICPF), is presented for the high-speed maneuvering targets with jerky motions. First, the velocity compensation and SKT are jointly employed to correct the RM. Second, an estimation method for CPS, named MICPF, is proposed and applied to compensate the DFM. Finally, the fast Fourier transform (FFT) and constant false alarm rate (CFAR) technique are employed to accomplish coherent integration and target detection, successively. Comparisons with the IAR-DCFT show that the SKT-MICPF can reduce the computational cost greatly with little detection performance loss.

The rest of this paper is organized as follows. In Sec. 2, the signal model for high-speed maneuvering targets with jerky motion is built. The SKT-based RM correction method is presented in Sec. 3. In Sec. 4, an MICPF method is proposed for CPS and its performances are also analyzed. A detection approach for high-speed maneuvering targets with jerky motion is illustrated in Sec. 5. In Sec. 6, the experiments with synthetic data and real data are performed to demonstrate the effectiveness of the proposed algorithm. Section 7 gives the conclusions.

2 Signal Model for High-Speed Maneuvering Targets

Suppose that the radar transmits a linear frequency modulation signal, which can be expressed as

$$s_i(t) = \text{rect}(t/T_r) \exp[j\pi(2f_c t + \gamma t^2)], \tag{1}$$

where $\text{rect}(\frac{t}{T_r}) = \begin{cases} 1, & |t| \leq T_r/2 \\ 0, & |t| > T_r/2 \end{cases}$, T_r is the pulse duration, and t , f_c , and γ denote the fast time, the carrier frequency, and the modulation rate, respectively.

Assume that there are P high-speed maneuvering targets with a constant radial jerk in the scene, thus the instantaneous slant range between the radar and the p 'th target satisfies

$$R_p(t_m) = r_p + v_p t_m + a_p t_m^2/2 + k_p t_m^3/6, \tag{2}$$

where t_m represents the slow time, and r_p , v_p , a_p , and k_p denote the initial slant range, the radial velocity, acceleration, and jerk of the p 'th target, respectively.

The received baseband echoes can be expressed as²

$$\begin{aligned} \mathbf{S}_r(t_m, t) &= \sum_{p=1}^P A_p \text{rect}\left(\frac{t - 2R_p(t_m)/c}{T_r}\right) \exp\left\{j\pi\gamma \left[t - \frac{2R_p(t_m)}{c}\right]^2\right\} \\ &\times \exp\left[-j2\pi f_c \frac{2R_p(t_m)}{c}\right] + \mathbf{N}(t_m, t), \quad t_m \in [-T/2, T/2], \end{aligned} \tag{3}$$

where A_p denotes the p 'th target reflectivity, and c and T represent the speed of light and the integration time, respectively. $\mathbf{N}(t_m, t)$ is the complex white Gaussian noise.

After the pulse compression, the echoes in the slow time-fast time domain can be stated as

$$\begin{aligned} \mathbf{S}_c(t_m, t) = & \sum_{p=1}^P A_{cp} \operatorname{sinc} \left\{ B \left[t - \frac{2(r_p + v_{Tp} t_m + a_p t_m^2/2 + k_p t_m^3/6)}{c} \right] \right\} \\ & \times \exp \left[-j2\pi \frac{2(r_p + v_{Tp} t_m + a_p t_m^2/2 + k_p t_m^3/6)}{\lambda} \right] + \mathbf{N}_c(t_m, t), \end{aligned} \quad (4)$$

where B denotes the bandwidth, $\mathbf{N}_c(t_m, t)$ is the compressed noise, and $\lambda = c/f_c$ is the wavelength.

3 Range Migration Correction

Performing the range FFT on Eq. (4), we get the compressed signal in the slow time range frequency domain.

$$\mathbf{S}_c(t_m, f_r) = \sum_{p=1}^P A_{1p} \operatorname{rect} \left(\frac{f_r}{B} \right) \exp \left[-j2\pi(f_c + f_r) \frac{2(r_p + v_{Tp} t_m + a_p t_m^2/2 + k_p t_m^3/6)}{c} \right], \quad (5)$$

where f_r denotes the range frequency.

In order to correct the RMs induced by the targets' radial velocities, a compensation function is constructed, which takes the form

$$\mathbf{H}_1(t_m, f_r, v_s) = \exp \left[j2\pi(f_c + f_r) \frac{2v_s t_m}{c} \right], \quad (6)$$

where v_s is the searching velocity.

Multiplying Eq. (6) with Eq. (5) yields

$$\begin{aligned} \mathbf{S}_1(t_m, f_r) = & \mathbf{H}_1(t_m, f_r, v_s) \times \mathbf{S}_c(t_m, f_r) \\ = & \sum_{p=1}^P A_{1p} \operatorname{rect} \left(\frac{f_r}{B} \right) \exp \left\{ -j2\pi(f_c + f_r) \frac{2[r_p + (v_{Tp} - v_s)t_m + a_p t_m^2/2 + k_p t_m^3/6]}{c} \right\}. \end{aligned} \quad (7)$$

To correct the RMs caused by the targets' radial accelerations, we perform the SKT on Eq. (7). The scaling equation of the SKT takes the form¹⁰

$$t_m = \left(\frac{f_c}{f_c + f_r} \right)^{1/2} t_n. \quad (8)$$

After the SKT, we get

$$\begin{aligned} \mathbf{S}_2(t_n, f_r) = & \sum_{p=1}^P A_{1p} \operatorname{rect} \left(\frac{f_r}{B} \right) \exp \left[-j2\pi(f_c + f_r) \frac{2r_p}{c} \right] \exp \left[-j2\pi f_c \left(1 + \frac{f_r}{f_c} \right)^{1/2} \frac{2(v_{Tp} - v_s)t_n}{c} \right] \\ & \times \exp \left(-j2\pi f_c \frac{a_p t_n^2}{c} \right) \exp \left[-j2\pi f_c \left(1 + \frac{f_r}{f_c} \right)^{-1/2} \frac{k_p t_n^3/3}{c} \right]. \end{aligned} \quad (9)$$

The SKT can be implemented via the FFT-based chirp-z transform with the computational cost of $O(MN \log_2 M)$,³ where M and N denote the number of integration pulses and range cells, respectively. For a narrowband radar, $f_c \gg f_r$ is true.¹¹ By using the first-order approximations $(1 + f_r/f_c)^{1/2} \approx 1 + f_r/(2f_c)$ and $(1 + f_r/f_c)^{-1/2} \approx 1 - f_r/(2f_c)$, Eq. (9) can be rewritten as

$$\begin{aligned} \mathbf{S}_2(t_n, f_r) &\approx \sum_{p=1}^P A_{1p} \text{rect}\left(\frac{f_r}{B}\right) \exp\left[-j2\pi(f_c + f_r) \frac{2r_p}{c}\right] \exp\left[-j2\pi\left(f_c + \frac{1}{2}f_r\right) \frac{2(v_{Tp} - v_s)t_n}{c}\right] \\ &\times \exp\left(-j2\pi f_c \frac{a_p t_n^2}{c}\right) \exp\left[-j2\pi\left(f_c - \frac{1}{2}f_r\right) \frac{k_p t_n^3/3}{c}\right]. \end{aligned} \quad (10)$$

Applying the inverse FFT (IFFT) on Eq. (10) along the f_r -axis, we get

$$\begin{aligned} \mathbf{S}_3(t_n, t) &\approx \sum_{p=1}^P A_{2p} \text{sinc}\left\{B\left[t - \frac{2[r_p + (v_{Tp} - v_s)t_n/2 - k_p t_n^3/12]}{c}\right]\right\} \\ &\times \exp\left\{-j2\pi \frac{2[r_p + (v_{Tp} - v_s)t_n + a_p t_n^2/2 + k_p t_n^3/6]}{\lambda}\right\}. \end{aligned} \quad (11)$$

From Eq. (11), it can be easily seen that the RMs induced by the targets' radial accelerations and part of the RMs caused by the targets' radial jerks have been corrected.

Assume that the radial velocity of the p 'th target is matched by the searching velocity, i.e., $|v_{Tp} - v_s| \leq \Delta v_s/2$, where Δv_s denotes the interval of the searching velocity. Therefore, the residual RM of the p 'th target satisfies

$$\left(\left|\frac{(v_{Tp} - v_s)}{2}t_n\right| - \frac{|k_p|}{12}t_n^3\right)\Big|_{t_n=\pm T/2} \leq \frac{\Delta v_s}{4}T + \frac{|k_p|_{\max}}{48}T^3. \quad (12)$$

The RMs induced by the targets' radial jerks are usually small for a narrowband radar.^{12,15} We limit the residual RMs induced by the targets' radial jerks to be half a range resolution in this paper. If the interval of searching velocity satisfies

$$\Delta v_s \leq 2\Delta R/T, \quad (13)$$

where $\Delta R = c/(2B)$ is the range resolution, the residual RM of the p 'th target will be less than a range resolution, which indicates that the RM effect can be ignored.² Thus, the interval of searching velocity can be selected in terms of Eq. (13).

With the searching procedure, all the targets can be corrected successively. However, the DFMs induced by the targets' radial accelerations and jerks still remain, which have a great impact on the integration performance.

4 Parameters Estimation of CPS Based on Modified Integrated Cubic Phase Function

In order to compensate the DFM, a modified ICPF is proposed for CPS and applied to compensate the DFM.

4.1 Modified Integrated Cubic Phase Function

Consider a monocomponent CPS expressed as follows:

$$\mathbf{s}(t_m) = \rho \exp\left[j2\pi\left(a_1 t_m + \frac{1}{2}a_2 t_m^2 + \frac{1}{6}a_3 t_m^3\right)\right], \quad t_m \in [-T/2, T/2], \quad (14)$$

where ρ , a_1 , a_2 , and a_3 denote the amplitude, the centroid frequency (CF), the CR, and the QCR, respectively. T represents the integration time.

The instantaneous frequency rate (IFR)^{22,23} of $\mathbf{s}(t_m)$ can be stated as

$$\text{IFR} = \frac{d^2\Phi(t_m)}{dt_m^2} = 2\pi(a_2 + a_3 t_m), \quad (15)$$

where $\Phi(t_m)$ denotes the phase of $\mathbf{s}(t_m)$.

The CPF^{22,23} is defined as

$$\begin{aligned} \text{CPF}(t_m, f) &= \int_{\tau_m^2} \mathbf{R}(t_m, \tau_m) \exp(-j2\pi f \tau_m^2) d\tau_m^2 \\ &= \rho_1 \exp\left[j2\pi\left(2a_1 t_m + a_2 t_m^2 + \frac{1}{3} a_3 t_m^3\right)\right] \delta(f - a_2 - a_3 t_m), \end{aligned} \quad (16)$$

where τ_m is a lag-time variable with respect to t_m , f denotes the IFR domain, and $\delta(\cdot)$ is the Dirac delta function. $\mathbf{R}(t_m, \tau_m)$ is the kernel function defined as

$$\begin{aligned} \mathbf{R}(t_m, \tau_m) &= \mathbf{s}(t_m + \tau_m) \mathbf{s}(t_m - \tau_m) \\ &= \rho^2 \exp\left[j2\pi\left(2a_1 t_m + a_2 t_m^2 + \frac{1}{3} a_3 t_m^3\right)\right] \exp[j2\pi(a_2 + a_3 t_m) \tau_m^2]. \end{aligned} \quad (17)$$

After the Fourier transform, the signal energy peaks along the inclined line $f - a_2 - a_3 t_m = 0$ in the time-IFR domain. The FT performed on Eq. (16) is with respect to τ_m^2 , which indicates that the unambiguous range of f is

$$|f| \leq f_s^2/2, \quad (18)$$

where f_s denotes the sampling frequency.

In realistic applications, the IFR of a CPS is usually much smaller than $f_s^2/2$.^{18-20,22-24} To obtain a higher estimation accuracy, we limit f to be $|f| \leq f_s/2$, and introduce a zoom factor to balance the resolution and range of the IFR. Thus, a modified CPF is defined as

$$\begin{aligned} \text{MCPF}(t_m, f_\tau) &= \int_{\tau_m^2} \mathbf{R}(t_m, \tau_m) \exp(-j2\pi f_\tau \eta \tau_m^2) d\tau_m^2 \\ &= \rho_1 \exp\left[j2\pi\left(2a_1 t_m + a_2 t_m^2 + \frac{1}{3} a_3 t_m^3\right)\right] \delta\left(f_\tau - \frac{a_2}{\eta} - \frac{a_3}{\eta} t_m\right), \quad f_\tau \in \left[-\frac{f_s}{2}, \frac{f_s}{2}\right], \end{aligned} \quad (19)$$

where η is the introduced zoom factor. The selection criterion will be discussed in Sec. 4.2.

Because the sampling corresponds to τ_m^2 is nonuniform, the Fourier transform performed on Eq. (19) cannot be implemented by the FFT. Fortunately, the nonuniform FFT (NUFFT) can be applied to speed up the FT with the computational cost of $O(M^2 \log_2 M)$,^{24,25} where M is the number of integration pulses.

After the NUFFT, the signal energy peaks along the inclined line

$$f_\tau - a_2/\eta - a_3 t_m/\eta = 0. \quad (20)$$

Due to the coupling between t_m and τ_m in the second exponential phase term of $\mathbf{R}(t_m, \tau_m)$, the inclined line is not parallel to the t_m -axis. Due to the first exponential phase term of $\mathbf{R}(t_m, \tau_m)$, the SCFT^{18,26} cannot remove this coupling. It is observed from Eq. (19) that, after the NUFFT operation, the CR and QCR have been packaged into the inclined line, i.e., Eq. (20).

The Radon transform,²⁷ the Hough transform,²⁸ and the modified Hough transform²⁹ are the effective methods to accomplish energy accumulation along a straight line. Nevertheless, a 2-D searching procedure is inevitable which will burden the system complexity and increase the computational cost.

To realize energy accumulation along the inclined line without brute-force searching, the IFFT is performed on $|\text{MCPF}(t_m, f_\tau)|^2$ with respect to f_τ

$$\mathbf{R}_1(t_m, \tau'_m) = \text{IFFT}_{f_\tau}[|\text{MCPF}(t_m, f_\tau)|^2] = \rho_2 \exp\left[j2\pi\left(\frac{a_2}{\eta} \tau'_m + \frac{a_3}{\eta} \tau'_m t_m\right)\right], \quad (21)$$

where τ'_m denotes the lag-time variable with respect to f_τ . $\text{IFFT}_{f_\tau}[\cdot]$ denotes the IFFT operation along the f_τ -axis. The first exponential phase term of $\mathbf{R}(t_m, \tau_m)$ does not appear in $\mathbf{R}_1(t_m, \tau'_m)$,

which indicates that the SCFT becomes applicable to remove the coupling between t_m and τ'_m . Applying the SCFT on Eq. (21) along the t_m -axis, we obtain

$$\mathbf{R}_2(f_t, \tau'_m) = \text{SCFT}_{(\xi\tau'_m t_m)}[\mathbf{R}_1(t_m, \tau'_m)] = \rho_3 \exp\left(j2\pi \frac{a_2}{\eta} \tau'_m\right) \delta\left(f_t - \frac{a_3}{\eta\xi}\right), \quad (22)$$

where f_t is the frequency domain with respect to $\tau'_m t_m$, $\text{SCFT}_{(\xi\tau'_m t_m)}[\cdot]$ denotes the SCFT operation along the t_m -axis, ξ is a zoom factor which is introduced to balance the resolution and range of the QCR, and its selection criterion will be analyzed in Sec. 4.2.

After the SCFT, the signal energy distributes along the beeline $f_t - a_3/\eta\xi = 0$ in the $\tau'_m - f_t$ domain. Thereafter, applying the FFT along the τ'_m -axis to achieve further energy accumulation, we obtain

$$\text{MICPF}(f_t, f'_\tau) = \text{FFT}_{\tau'_m}[\mathbf{R}_2(f_t, \tau'_m)] = \rho_4 \delta\left(f'_\tau - \frac{a_2}{\eta}\right) \delta\left(f_t - \frac{a_3}{\eta\xi}\right), \quad (23)$$

where $\text{FFT}_{\tau'_m}[\cdot]$ denotes the FFT operation along the τ'_m -axis.

A sole peak has been accumulated at the point $[a_2/\eta, a_3/(\eta\xi)]$ in the $f'_\tau - f_t$ domain. Thereafter, a peak detection technique^{18-20,24} is employed to estimate the CR and QCR of the CPS.

From the above discussion, the abbreviated expression of the proposed MICPF can be expressed as

$$\text{MICPF}(f_t, f'_\tau) = \text{FFT}_{\tau'_m} \{ \text{SCFT}_{(\xi\tau'_m t_m)} \{ \text{IFFT}_{f_t} [\text{NUFFT}_{(\eta\tau'_m)} [\text{KF}(\mathbf{s}(t_m))]]^2 \} \}, \quad (24)$$

where $\text{KF}[\cdot]$ denotes the kernel function defined in Eq. (17).

4.2 Selection Criteria of Zoom Factors

Equation (23) indicates that the CR and QCR of the CPS can be estimated as

$$a_2 = \eta \hat{f}'_\tau, |\hat{f}'_\tau| \leq f_s/2, \quad (25)$$

$$a_3 = \eta\xi \hat{f}_t, |\hat{f}_t| \leq f_s/2, \quad (26)$$

where $(\hat{f}_t, \hat{f}'_\tau)$ denotes the peak location. Furthermore, the estimated ranges of the CR and QCR are

$$|a_2| \leq \eta f_s/2, \quad (27)$$

$$|a_3| \leq \eta\xi f_s/2. \quad (28)$$

To avoid spectrum aliasing, it is assumed that $|a_2| \leq f_s/T, |a_3| \leq (9f_s)/(2T^2)$,^{22,23} thus we have

$$|a_2 + a_3 t_m| \leq 13f_s/(4T). \quad (29)$$

In order to avoid energy loss, Eq. (19) indicates that η should satisfy

$$|(a_2 + a_3 t_m)/\eta| \leq f_s/2. \quad (30)$$

Therefore, η should be

$$\eta \geq 6.5/T. \quad (31)$$

Equations (27) and (31) indicate that the estimated range of the CR is larger than its unambiguous range, so it is suitable for the CR estimation. Similarly, the estimated range of the QCR should be larger than its unambiguous range, which indicates that ξ should be

$$\xi \geq 9/(\eta T^2). \quad (32)$$

However, a bigger zoom factor will result in resolution degradation. Therefore, we suggest $\eta = 6.5/T$, $\xi = 18/(13T)$ for the MICPF.

In realistic applications, the CR and QCR of a CPS may be limited to a smaller range. Under this situation, the zoom factors can be selected in terms of the real ranges of the parameters.

4.3 Performance Analyses

The cross-term suppression performance, the computational complexity, and the antinoise performance are analyzed to evaluate the performance of the proposed MICPF. The SCFT-based method,¹⁸ the SS-ICPF,²⁴ and the method in Ref. 30 are also presented for comparison. These are chosen due to the following: (1) these three approaches are the typical methods for the parameters estimation of the CPS, (2) no or few redundant data is necessary, and (3) the CR and QCR are estimated simultaneously, which can suppress the error propagation.

4.3.1 Cross-term suppression performance

The bilinearity of the MICPF indicates that cross-terms will appear for multi-CPS. After the NUFFT, the cross-terms in the time-IFR domain take the cosine oscillation structure.²⁴ Thus, the cross-terms cannot be accumulated as the self-terms, because: (1) MICPF can achieve energy accumulation along the inclined line with where signal energy peaks, and (2) the cosine oscillation structure will spread the cross-terms energy. This conclusion can be proven by the experiment performed in Sec. 6.1.

However, if the amplitudes of different CPSs differ significantly, the weak CPSs may be submerged by the cross-terms generated by the strong CPSs. Under this situation, similar to other estimation methods,¹⁸⁻²⁰ the CLEAN technique³¹ can be employed to separate the weak and strong CPSs, then the strong CPSs and weak CPSs can be estimated iteratively.

4.3.2 Computational complexity

In what follows, the computational complexity is analyzed in terms of the number of operations, i.e., complex multiplications (Mc) and complex additions (Ac). Denote the sampling points of signal by M . The main procedures of the MICPF include: the NUFFT-based FT performed on Eq. (19) [$O(M^2 \log_2 M)$ Mc and $O(M^2 \log_2 M)$ Ac], the IFFT applied on Eq. (21) [$O(M^2 \log_2 M)$ Mc and $O(M^2 \log_2 M)$ Ac], the chirp-z-based SCFT taken of Eq. (22) [$O(M^2 \log_2 M)$ Mc and $O(M^2 \log_2 M)$ Ac], and the FFT performed on Eq. (23) [$O(M^2 \log_2 M)$ Mc and $O(M^2 \log_2 M)$ Ac]. On the other hand, $O(M^2 \log_2 M)$ Mc and $O(M^3)$ Ac are needed for the SS-ICPF,²⁴ and $O(M^2 \log_2 M)$ Mc and $O(M^2 \log_2 M)$ Ac are needed for the SCFT-based method¹⁸ and the method in Ref. 30. The computational costs of the MICPF, the SS-ICPF, the SCFT-based method, and the method in Ref. 30 are listed in Table 1.

It can be seen from Table 1 that the computational complexity of the proposed method is lower than that of the SS-ICPF. Moreover, for the SS-ICPF, the space switch method which includes a circular shifting operation and map operation will burden the complexity of the

Table 1 Computational cost.

Methods	Multiplications	Additions
MICPF	$O(M^2 \log_2 M)$	$O(M^2 \log_2 M)$
SS-ICPF	$O(M^2 \log_2 M)$	$O(M^3)$
SCFT-based	$O(M^2 \log_2 M)$	$O(M^2 \log_2 M)$
Ref. 30	$O(M^2 \log_2 M)$	$O(M^2 \log_2 M)$

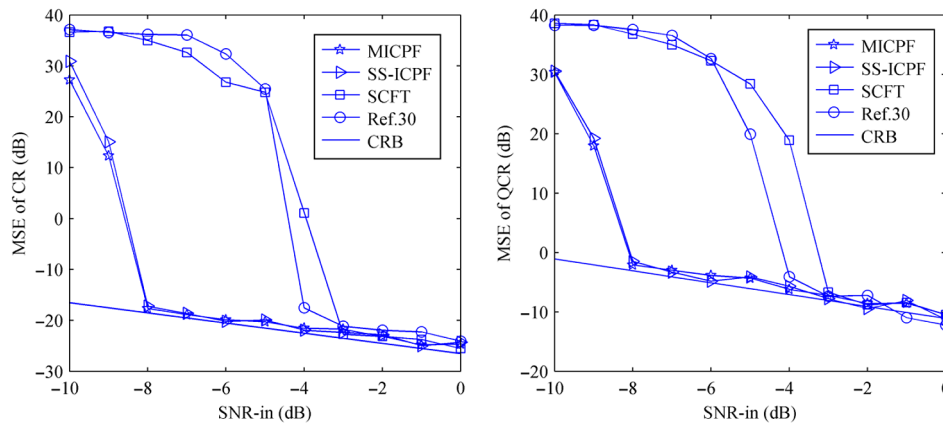


Fig. 1 Parameters estimation performance: (a) MSE of the CR estimation and (b) MSE of the quadratic CR estimation.

estimator.^{24,29} The computational cost of the MICPF, the SCFT-based method, and the method in Ref. 30 are in the same order. However, the antinoise performance of the MICPF is better than that of the SCFT-based method and the method in Ref. 30, which will be analyzed in Sec. 4.3.3.

4.3.3 Antinoise performance

First-order perturbation analysis as used in Ref. 21 is an effective method to analyze the antinoise performance of estimation algorithms. However, due to the NUFFT operation, the modulus square operation, the IFFT operation, the SCFT operation, and the FFT operation that are performed on $\mathbf{R}(t_m, \tau_m)$, the first-order perturbation analysis becomes extremely difficult. Similar to Refs. 18–20, the mean square error (MSE) is adopted to analyze the antinoise performance of MICPF in this section.

Example: Consider a mono-CPS contaminated with a zero-mean complex white Gaussian noise, where the sampling frequency and sampling points of the signal are 128 Hz and 256, respectively. The CF, CR, and QCR of the CPS are set as 40 Hz, 60 Hz/s, and 50 Hz/s², respectively, and the test input SNRs are $[-10:1:0]$ (dB). 100 iterations of Monte-Carlo experiments are performed for each input SNR value. The zoom factors η and ξ are set as 2 and 0.5, respectively. It is worthwhile noting that the zoom factors are set in terms of the parameters' actual values. However, it is not in conflict with the selection criteria described in Sec. 4.2. Moreover, in Sec. 6, the zoom factors are also set in terms of the real ranges of the targets' motion parameters.

The simulation results and the corresponding Cramer–Rao bounds (CRBs) are shown in Fig. 1, and the expressions of the CRBs can be found in Ref. 32. In Fig. 1, the threshold SNR of the MICPF is -8 dB, because: (1) the bilinear kernel function is applied in the MICPF and (2) signal energy is well accumulated by the proposed nonsearching method. The SS-ICPF has the same antinoise performance as the MICPF, but with a greater computational cost. However, the threshold SNR of the SCFT-based method is -3 dB due to the fourth-order nonlinear kernel function being applied. Compared with the SCFT-based method, the method in Ref. 30 introduces a constant delay to suppress noise, and achieves a 1 dB antinoise performance gain. Nevertheless, it still has a 4 dB loss compared with the MICPF.

From the above analyses and experiments, we can conclude that the proposed method is more suitable for CPS than the SS-ICPF, the SCFT-based method, and the method in Ref. 30.

5 Target Detection Based on Second-Order Keystone Transform Modified Integrated Cubic Phase Function

In this section, by employing the SKT-based RM correction method and the MICPF, a coherent detection algorithm, known as SKT-MICPF, is presented to realize the detection of a high-speed maneuvering target with a constant radial jerk.

5.1 Target Detection Based on Second-Order Keystone Transform Modified Integrated Cubic Phase Function

For simplicity, a single target is considered in the scene. After the RM correction with the proposed method in Sec. 3, the azimuth echoes of a range cell where a target is located can be stated as

$$s(t_n) = A_1 \exp\left\{-j2\pi \frac{2[r + (v_T - v_s)t_n + at_n^2/2 + kt_n^3/6]}{\lambda}\right\}. \tag{33}$$

Performing the MICPF on $s(t_n)$, we get

$$\text{MICPF}(f_t, f'_t) = A_2 \delta\left(f'_t + \frac{2a}{\lambda\eta}\right) \delta\left(f_t + \frac{2k}{\lambda\eta\xi}\right). \tag{34}$$

Target's radial acceleration and jerk can be estimated via peak detection technique. Thus, a compensation function is constructed to compensate the DFM, which takes the form

$$\mathbf{H}_2(\hat{a}, \hat{k}, t_n) = \exp\left[j2\pi\left(\frac{\hat{a}}{\lambda}t_n^2 + \frac{\hat{k}}{3\lambda}t_n^3\right)\right], \tag{35}$$

where \hat{a} and \hat{k} denote the estimated acceleration and jerk, respectively.

After the DFM compensation, the FFT is applied to achieve coherent integration

$$s(f_d) = \text{FFT}_{t_n}\{s(t_n) \times \mathbf{H}_2(\hat{a}, \hat{k}, t_n)\} = A_3 \exp\left(-j2\pi \frac{2r}{\lambda}\right) \delta\left(f_d + \frac{2V}{\lambda}\right), \tag{36}$$

where $V = v_T - v_s$.

The processing procedures of the proposed method, i.e., velocity compensation, SKT, and DFM compensation, will not change the distributions. Therefore, the CFAR technique is utilized to target detection, and the threshold can be set as³³

$$\hat{T} = N_w(P_{\text{FA}}^{-1/N_w} - 1)\hat{\beta}^2, \tag{37}$$

where N_w , P_{FA} , and $\hat{\beta}^2$ denote the length of the reference windows, the probability of false alarm, and the estimated noise power, respectively.

It is worth noting that the strong target may be detected even when the RM has not been completely corrected, i.e., different search velocities yield positive detections. Under this situation, we confirm that the target's radial velocity has been matched by the searching velocity, if both of the following two criteria are satisfied: (1) the searching velocity satisfies $|\hat{V}| \leq \Delta v_s/2$, where \hat{V} denotes the estimated value of V ; and (2) the searching velocity corresponds to the best integration result (the maximum integrated peak).

By the criterion 1, the range of searching velocity has been confined to $v_{sn} = v_{s0} + nv_a (n = 0, \pm 1, \pm 2, \dots)$, where v_{s0} denotes the searching velocity which matches the target's radial velocity v_T , i.e., $|v_T - v_{s0}| \leq \Delta v_s/2$. Thereafter, the criterion 2 is introduced to select v_{s0} among $v_{sn} = v_{s0} + nv_a (n = 0, \pm 1, \pm 2, \dots)$. On one hand, the RM can be completely corrected when the searching velocity is v_{s0} , then optimal integration can be obtained. On the other hand, due to the long-time integration, $v_a T > \Delta R$ can be easily satisfied, which indicates that the RM cannot be completely removed when the searching velocities are $v_{sn} = v_{s0} + nv_a (n = \pm 1, \pm 2, \dots)$, and will result in integration loss. Therefore, criterion 2 implies that the final matched velocity can be selected from the set of v_{sn} .

Furthermore, the target's radial velocity can be estimated as

$$\hat{v}_T = v_{s0} + \hat{V}. \tag{38}$$

Although a single target is considered in the above analysis, SKT-MICPF has a good detection performance for multitargets since it can distinguish multitargets from the initial range, the radial velocity, acceleration, and jerk.

5.2 Procedure of Second-Order Keystone Transform Modified Integrated Cubic Phase Function

The flowchart of the SKT-MICPF is shown in Fig. 2, which is mainly composed of seven steps. I and N denote the number of searching velocities and range cells, respectively.

- Step 1: Complete the downconversion, pulse compression, and range FFT. Initialize the range of the searching velocity, let $i = 1$.
- Step 2: Construct the i 'th compensation function $\mathbf{H}_1(t_m, f_r, v_{si})$ as Eq. (6), and multiply $\mathbf{H}_1(t_m, f_r, v_{si})$ with $\mathbf{S}_c(t_m, f_r)$. Thereafter, the SKT and range IFFT are performed successively. Initialize the range of searching range cell, let $n = 1$.
- Step 3: Get the data $\mathbf{s}(t_n)$ of the n 'th range cell, and perform the MICPF on $\mathbf{s}(t_n)$. Carry out the peak detection in the $f_t - f'_t$ domain. If a peak has been detected, estimate the acceleration and jerk, and then go to step 4. Otherwise, go to step 5.
- Step 4: Construct a compensation function $\mathbf{H}_2(\hat{a}, \hat{k}, t_n)$ as Eq. (35), and multiply $\mathbf{H}_2(\hat{a}, \hat{k}, t_n)$ with $\mathbf{s}(t_n)$. Accomplish coherent integration and target detection via the FFT and CFAR detection, successively. If a target has been detected, estimate V , and note down the coordinate, then go to step 5. Otherwise, go directly to step 5.
- Step 5: If $n < N$, set $n = n + 1$, and repeat step 3 and step 4 until $n = N$.
- Step 6: If $i < I$, set $i = i + 1$, and repeat step 2 to step 5 until $i = I$.
- Step 7: After all the searching velocities and range cells have been detected, estimate targets' radial velocities by the two criteria in Sec. 5.1.

5.3 Analysis of Computational Complexity

Denote the number of searching velocities, integration pulses, and range cells by I , M , and N , respectively. Assume that the number of searching angles of IAR-DCFT is I . The main procedures of the SKT-MICPF include: I times chirp-z-based SKT [$O(MNI \log_2 M)$], MI times N points IFFT [$O(MNI \log_2 N)$], and NI times MICPF [$O(M^2NI \log_2 M)$]. Therefore, the computational cost of the SKT-MICPF is $O(M^2NI \log_2 M)$. On the other hand, the computational cost of the IAR-DCFT is $O(M^3NI \log_2 M)$.¹⁵

From the above analysis, we can see that the computational complexity of the proposed method is much less than that of the IAR-DCFT. In real applications, the initial slant range

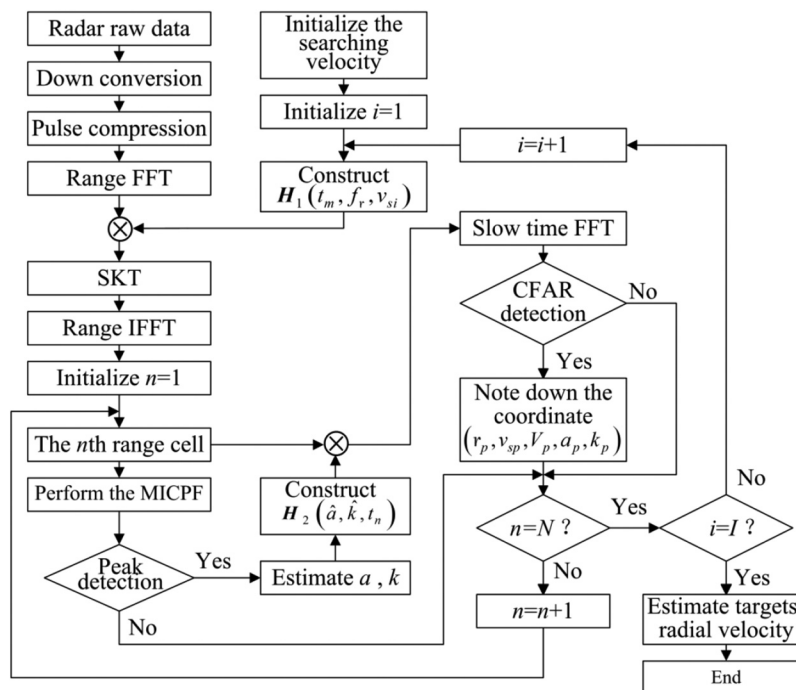


Fig. 2 Flowchart of the SKT-MICPF.

and radial velocity of a target are limited to some fixed region via prior knowledge,⁶ and the computational cost of the proposed method can be further decreased.

Remark: Although the SKT-MICPF is proposed for high-speed maneuvering targets' detection, it can also be applied to inverse synthetic aperture radar (ISAR) imaging. For ISAR imaging of a target with complex motion, after the range alignment and the phase adjustment, the azimuth echoes of a range cell can be modeled as multi-CPS.^{17–20,24,30} If the parameters of those CPSs can be estimated, high-resolution imaging can be obtained. Moreover, the performance of parameters' estimation has a great impact on the imaging quality. The proposed MICPF can achieve high-precision estimation for multi-CPS. Comparisons with the SS-ICPF, the SCFT-based method, and the method in Ref. 30 show that the proposed MICPF outperforms those methods, which indicates that the proposed MICPF can also be applied to ISAR imaging, and may achieve a better imaging quality than those methods.

6 Verification of the Proposed Algorithm

We are to validate the effectiveness of the proposed detection algorithm with synthetic radar data and real radar data.

6.1 Verification with Synthetic Radar Data

Two high-speed maneuvering targets with a constant radial jerk are contained in the radar echoes. The radar parameters and targets' motion parameters are listed in Tables 2 and 3, respectively. The echoes are contaminated with a zero-mean complex white Gaussian noise.

Assume the ranges of the targets' radial acceleration and jerk are limited to $[-50,50]$ m/s^2 and $[-40,40]$ m/s^3 , respectively. The zoom factor of the MICPF can be set as $\eta = 1.2$, $\xi = 0.5$ in terms of the radar parameters and the ranges of the target's motion parameters. According to the above parameters, the estimated resolutions of acceleration and jerk are 0.09 m/s^2 and 0.045 m/s^3 , respectively. The SNRs (after the pulse compression) of the two targets are $\text{SNR}_A = -3$ dB and $\text{SNR}_B = -6$ dB. The interval of the searching velocity is set as 15 m/s for the RM correction in terms of Eq. (13).

Figure 3 shows the simulation results of the SKT-MICPF. The result after the pulse compression is given in Fig. 3(a). Because of the low SNR, the two targets are buried in the noise.

Table 2 Radar parameters of the synthetic data.

Parameter (unit)	Values
Carrier frequency (GHz)	1
Pulse width (μs)	50
Bandwidth (MHz)	10
Sample frequency (MHz)	10
PRF (Hz)	1000
Number of integrated pulses	2000

Table 3 Targets' motion parameters.

Target	Range cell index	Radial velocity (m/s)	Radial acceleration (m^2/s)	Radial jerk (m^3/s)
A	200	2097	45	-36
B	200	2106	-42	31.5

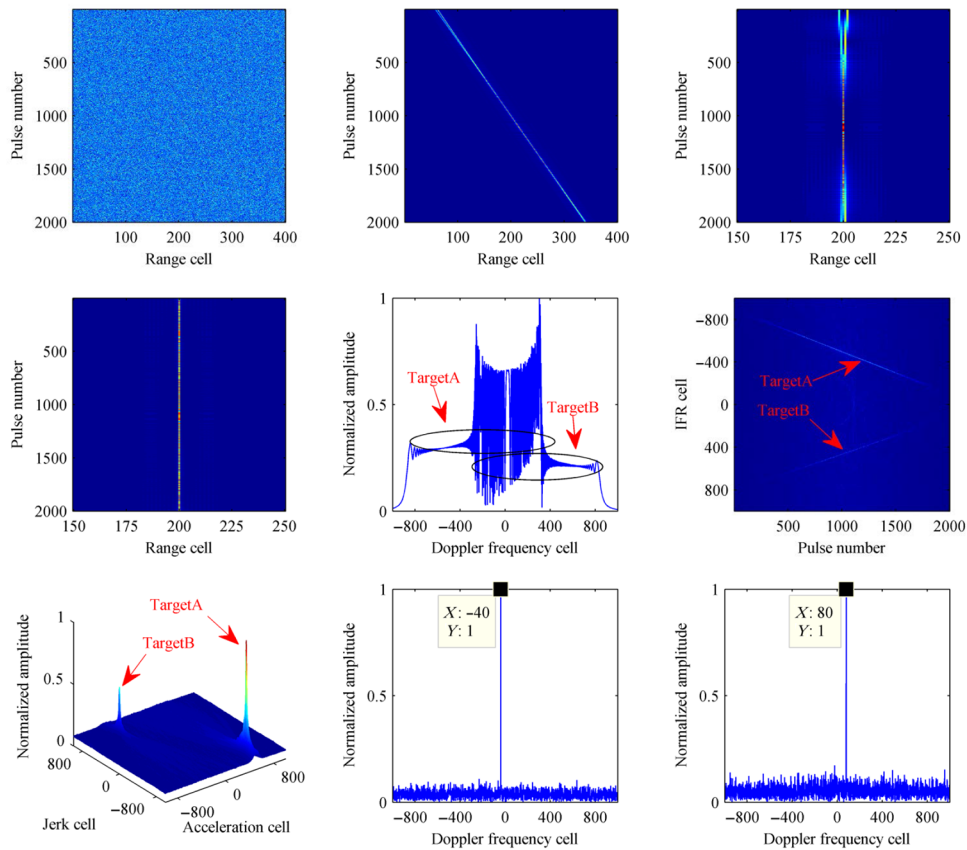


Fig. 3 Simulation results of the SKT-MICPF [(b)–(e) without noise]: (a) result after the pulse compression, (b) result after the pulse compression without noise, (c) result after the velocity compensation (the searching velocity is 2100 m/s), (d) result after the SKT, (e) result after the FFT performed on the 200th range cell, (f) the distribution of targets energy in the slow time-IFR domain, (g) result of the MICPF, (h) coherent integration result of target A after the RM and DFM compensation, and (i) coherent integration result of target B after the RM and DFM compensation.

Figure 3(b) shows the result after the pulse compression without noise. Due to the high-speed, serious RMs occur to the two targets. The results after the velocity compensation (2100 m/s) and the SKT are shown in Figs. 3(c) and 3(d), respectively. The RMs of the two targets have been corrected. Although the RMs have been corrected, the DFMs still remain, which make the targets' energy spread in the Doppler frequency domain as shown in Fig. 3(e). The distribution of the targets' energy in the slow time-IFR domain is shown in Fig. 3(f). The two targets peak along two inclined lines in the slow time-IFR domain, respectively. Figure 3(g) gives the accumulation result via the proposed method. Two peaks have been accumulated and well distinguished in the acceleration-jerk domain, whereas the cross-term is not accumulated. Thus, the targets' radial accelerations and jerks can be estimated by the peak detection technique. Figures 3(h) and 3(i) show the coherent integration results after the RM and DFM compensation. Targets are well-concentrated and can be easily detected via the CFAR technique.

If there is another target (target C) with a radial velocity, e.g., 2000 m/s, it is also located in the 200th range cell. Assume that the searching velocities are set as [1800:15:2400] m/s. When the searching velocity is 1995 m/s, the RM of target C can be completely compensated, whereas serious RMs still remain for targets A and B. Therefore, target C can be detected first. When the searching velocity is 2100 m/s, the RMs of targets A and B can be eliminated further to parameters estimation and targets detection.

The integration results of the RFT,² RLVD,⁷ IAR-DCFT,¹⁵ and the proposed SKT-MICPF are further performed for comparison. Consider target A in the scene, where the SNR after the pulse compression is set as -13 dB.

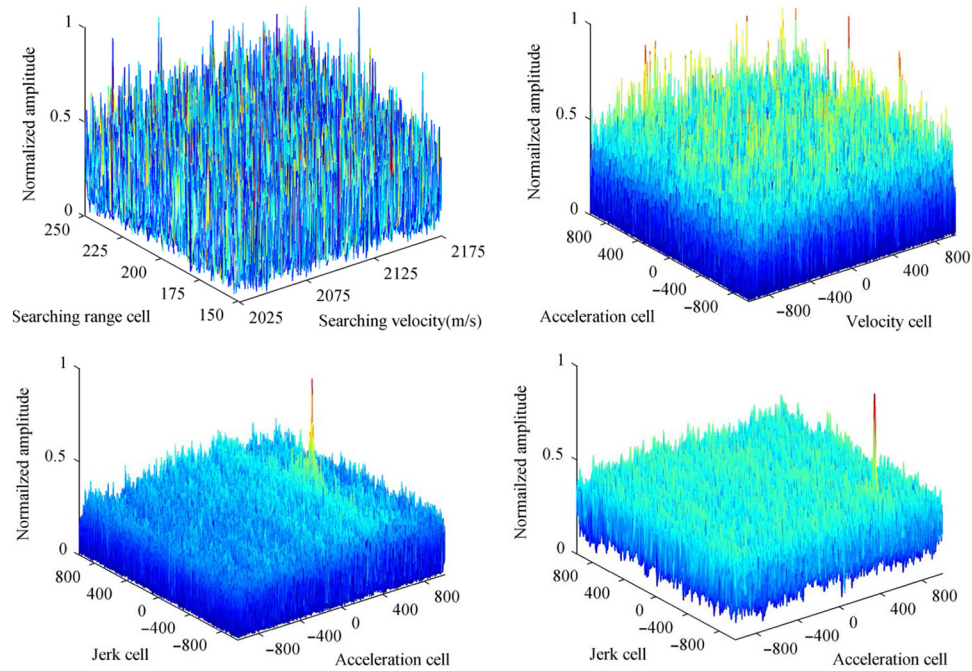


Fig. 4 Integration results of the RFT, RLVD, IAR-DCFT, and SKT-MICPF: (a) integration result of the RFT, (b) integration result of the RLVD, (c) integration result of the IAR-DCFT, and (d) integration result of the SKT-MICPF.

Figure 4(a) shows the integration result via the RFT. Because of the RM and DFM induced by the target's radial acceleration and jerk, RFT becomes invalid. The integration result of the RLVD is given in Fig. 4(b). The RM induced by the target's radial velocity and acceleration and the DFM caused by the target's radial acceleration can be eliminated by the RLVD. However, the DFM induced by the target's radial jerk affects the integration performance. The integration results of the IAR-DCFT and SKT-MICPF are shown in Figs. 4(c) and 4(d), respectively. The target is well-focused via the two approaches, which indicates that the IAR-DCFT and SKT-MICPF are suitable for the detection of a high-speed maneuvering target with a jerky motion. However, the SKT-MICPF has a lower computational complexity, which has been analyzed in Sec. 5.3. The time costs of the SKT-MICPF and IAR-DCFT are also given in Table 4.

The detection performances of the RFT, RLVD, IAR-DCFT, and SKT-MICPF are further evaluated by Monte-Carlo experiments, and target A is considered in the scene. The false alarm rate is set to be 10^{-6} , the test input SNRs are $[-25:1:20]$ (dB, after the pulse compression), and 100 Monte-Carlo experiments are performed for each input SNR value. The simulation results are shown in Fig. 5.

It is observed from Fig. 5 that, due to its ability to deal with the DFM effect induced by the target's radial jerk, the detection performance of the proposed method is superior to those of the RFT and RLVD. The IAR-DCFT has a better detection performance (2 dB) than the SKT-MICPF. This is because: (1) the DCFT has the optimal antinoise performance^{16,17} and (2) the MICPF suffers from SNR loss due to its bilinearity. However, the computational cost of the IAR-DCFT is much greater than that of the SKT-MICPF.

Table 4 Time cost of the SKT-MICPF and IAR-DCFT.

Algorithms	Time cost (s)
SKT-MICPF	34.4294
IAR-DCFT	1682.7359

Main configuration of the computer: CPU: Intel Core i7-4770 3.4 GHz;
RAM: 8.00 GHz; operating system: Windows 7; software: MATLAB[®] 2012a.

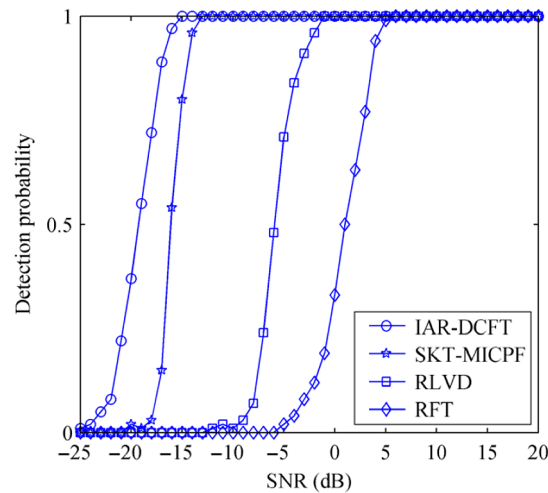


Fig. 5 Detection probability curves against input SNR.

From the above experiments, we can see that the SKT-MICPF offers a much better performance than the RFT and RLVD, while offering a much lower computational cost than the higher performing IAR-DCFT. This makes the proposed approach a stronger candidate for practical adoptions.

6.2 Verification with Real Radar Data

The real radar data were collected in February 2010 by the National University of Defense Technology, Hunan, China. The parameters of the radar system are listed in Table 5. The 2000 integration pulses and 200 range cells are extracted from the collected data.

According to Eq. (13), the interval of the searching velocity is set as 30 m/s for the RM correction. The processing results are shown in Fig. 6.

Figures 6(a) and 6(b) show the original radar echoes and the result after the pulse compression, respectively. It is obvious from Fig. 6(b) that the target envelope has been shifted away from its original position due to the RM. Figure 6(c) gives the result of RM correction via the proposed method (the searching velocity is -180 m/s). After the velocity compensation and SKT, the RM has been corrected. The result after the MICPF performed on the 121th range cell is shown in Fig. 6(d). We can see that a peak has been accumulated, and then the target's radial acceleration and jerk can be estimated by the peak detection technique. Figure 6(e) gives the integration result via the MTD, and the nearby area of the integrated peak is also zoomed-in to evaluate the integration performance. Due to the RM and DFM, target energy distributes in both the range and Doppler directions. The integration result of the proposed method is shown in Fig. 6(f). Because the proposed method can compensate the RM and DFM, the integrated peak of the proposed SKT-MICPF is larger than that of the MTD.

Although the maneuverability and velocity of the passenger plane are low, the RM and DFM affect the integration performance greatly. The advantages of the SKT-MICPF will be more obvious for a target moving at a higher speed and maneuverability.

Table 5 Radar parameters of the real data.

Parameter (unit)	Values
Wave band	L
Pulse width (μs)	75
Bandwidth (MHz)	2
Sample frequency (MHz)	3.25
PRT (μs)	910

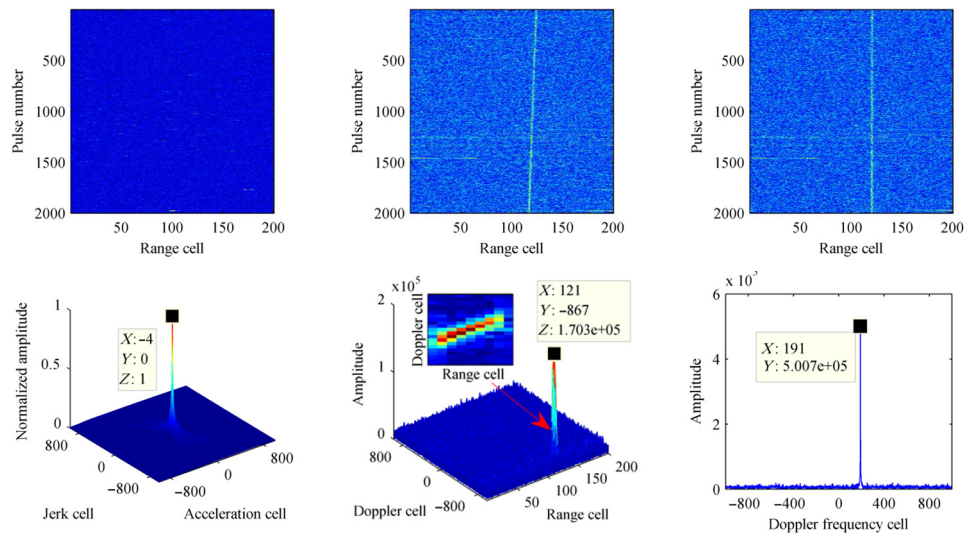


Fig. 6 Processing results of real radar data via the SKT-MICPF: (a) radar echoes, (b) pulse compression result, (c) RM correction result (the searching velocity is -180 m/s), (d) MICPF result, (e) integration result via the MTD (the zoomed-in area: range cell: $[117:125]$, Doppler cell: $[-877: -857]$), and (f) coherent integration result via the SKT-MICPF.

7 Conclusions

In this paper, an SKT-based RM correction method is first proposed then an MICPF is presented for the parameters' estimation of CPS. Thereafter, by using the proposed RM correction method and MICPF, a coherent target detection algorithm, known as SKT-MICPF, is proposed for a high-speed maneuvering target with a constant jerkiness. The advantages of the proposed method include the following: (1) the estimations of a target's radial acceleration and jerk are not searched which greatly reducing the computational cost; (2) the RM correction and DFM compensation can be accomplished in a low SNR scene, which indicates the proposed method can get a high antinoise performance; and 3) it has a good detection performance for multitargets since it can distinguish multitargets from the initial slant range, radial velocity, radial acceleration, and radial jerk. Comparisons with several methods show that the SKT-MICPF offers a much better performance than the RFT and RLVD, while offering a much lower computational cost than the higher performing IAR-DCFT. This makes the proposed approach a stronger candidate in realistic applications.

Acknowledgments

This work was partially supported by the National Natural Science Foundation of China (61001204) and the Fundamental Research Funds for the Central Universities (JY0000902020). Jiancheng Zhang and Tao Su proposed the target detection algorithms and wrote this paper; Jiancheng Zhang and Yanyan Li performed the experiments; Jibin Zheng analyzed the data and revised the article.

References

1. M. Xing et al., "New parameter estimation and detection algorithm for high speed small target," *IEEE Trans. Aerosp. Electron. Syst.* **47**(1), 214–224 (2011).
2. J. Xu et al., "Radon-Fourier transform for radar target detection I: generalized Doppler filter bank," *IEEE Trans. Aerosp. Electron. Syst.* **47**(2), 1186–1202 (2011).
3. D. Zhu, Y. Li, and Z. Zhu, "A keystone transform without interpolation for SAR ground moving-target imaging," *IEEE Geosci. Remote Sens. Lett.* **4**(1), 18–22 (2007).
4. X. Rao et al., "Axis rotation MTD algorithm for weak target detection," *Digital Signal Process.* **26**, 81–86 (2014).

5. J. Zheng et al., "Radar high-speed target detection based on the scaled inverse Fourier transform," *IEEE J. Sel. Top. Appl. Earth Obs. Remote Sens.* **8**(3), 1108–1119 (2015).
6. X. Chen et al., "Maneuvering target detection via Radon-fractional Fourier transform-based long-time coherent integration," *IEEE Trans. Signal Process.* **62**(4), 939–953 (2014).
7. X. Li et al., "Coherent integration for maneuvering target detection based on Radon-Lv's distribution," *IEEE Signal Process. Lett.* **22**(9), 1467–1471 (2015).
8. J. Tian et al., "Joint estimation algorithm for multi-targets' motion parameters," *IET Radar Sonar Navig.* **8**(8), 939–945 (2014).
9. S. Zhu et al., "A new method for radar high-speed maneuvering weak target detection and imaging," *IEEE Geosci. Remote Sens. Lett.* **11**(7), 1175–1179 (2014).
10. J. Tian, W. Cui, and S. Wu, "A novel method for parameter estimation of space moving targets," *IEEE Geosci. Remote Sens. Lett.* **11**(2), 389–393 (2014).
11. L. Kong et al., "Coherent integration algorithm for a maneuvering target with high-order range migration," *IEEE Trans. Signal Process.* **63**(17), 4474–4486 (2015).
12. P. Huang et al., "Approach for space-based radar manoeuvring target detection and high-order motion parameter estimation," *IET Radar Sonar Navig.* **9**(6), 732–741 (2015).
13. X. Li et al., "A low complexity coherent integration method for maneuvering target detection," *Digital Signal Process.* **49**, 137–147 (2016).
14. X. Li et al., "A fast detection method for maneuvering target in coherent radar," *IEEE Sensors J.* **15**(11), 6722–6729 (2015).
15. X. Rao et al., "Long-time coherent integration detection of weak manoeuvring target via integration algorithm, improved axis rotation discrete chirp-Fourier transform," *IET Radar Sonar Navig.* **9**(7), 917–926 (2015).
16. X. Xia, "Discrete chirp-Fourier transform and its application to chirp rate estimation," *IEEE Trans. Signal Process.* **48**(11), 3122–3133 (2000).
17. L. Wu et al., "ISAR imaging of target with complex motion based on discrete chirp Fourier transform for cubic chirp," *IEEE Trans. Geosci. Remote Sens.* **50**(10), 4201–4212 (2012).
18. X. Bai et al., "ISAR imaging of a ship target based on parameter estimation of multi-component quadratic frequency-modulated signals," *IEEE Trans. Geosci. Remote Sens.* **52**(2), 1418–1429 (2014).
19. J. Zheng et al., "ISAR imaging of targets with complex motions based on the keystone time-chirp rate distribution," *IEEE Geosci. Remote Sens. Lett.* **11**(7), 1275–1279 (2014).
20. Y. Li, T. Su, and J. Zheng, "Inverse synthetic aperture radar imaging of targets with complex motion based on modified chirp rate-quadratic chirp rate for cubic phase signal," *J. Appl. Remote Sens.* **9**, 095036 (2015).
21. P. Wang et al., "Integrated cubic phase function for Linear FM signal analysis," *IEEE Trans. Aerosp. Electron. Syst.* **46**(3), 963–977 (2010).
22. P. O'shea, "A fast algorithm for estimating the parameters of a quadratic FM signal," *IEEE Trans. Signal Process.* **52**(2), 385–393 (2004).
23. P. O'shea, "A new technique for instantaneous frequency rate estimation," *IEEE Signal Process. Lett.* **9**(8), 251–252 (2002).
24. J. Zheng et al., "ISAR imaging for fluctuating ships based on a fast bilinear parameter estimation algorithm," *IEEE J. Sel. Top. Appl. Earth Obs. Remote Sens.* **8**(8), 3954–3966 (2015).
25. Q. Liu and N. Nguyen, "An accurate algorithm for non uniform fast Fourier transforms (NUFFT's)," *IEEE Microwave Guided Wave Lett.* **8**(1), 18–20 (1998).
26. Y. Li et al., "Inverse synthetic aperture radar imaging of targets with nonsevere maneuverability based on the centroid frequency chirp rate distribution," *J. Appl. Remote Sens.* **8**, 095065 (2015).
27. J. Carretero-moya et al., "Application of the Radon transform to detect small-targets in sea clutter," *IET Radar Sonar Navig.* **3**(2), 155–166 (2009).
28. B. Carlso, E. D. Evans, and S. L. Wilson, "Search radar detection and track with the Hough transform," *IEEE Trans. Aerosp. Electron. Syst.* **30**(1), 102–108 (1992).
29. J. Zeng et al., "Modified Hough transform for searching radar detection," *IEEE Geosci. Remote Sens. Lett.* **5**(4), 683–686 (2008).

30. J. Zheng et al., "ISAR imaging of targets with complex motions based on a noise-resistant parameter estimation algorithm without nonuniform axis," *IEEE Sensors J.* **8**(16), 2509–2518 (2016).
31. J. Misiurewicz et al., "Radar detection of helicopters with application of CLEAN method," *IEEE Trans. Aerosp. Electron. Syst.* **48**(4), 3525–3537 (2012).
32. B. Ristic and B. Boashash, "Comments on 'The Cramer-Rao lower bounds for signals with constant amplitude and polynomial phase'," *IEEE Trans. Signal Process.* **46**(6), 1708–1709 (1998).
33. M. Richards, *Fundamentals of Radar Signal Processing*, pp. 352–354, McGraw-Hill, New York (2005).

Jiancheng Zhang received his BS degree in measurement and control technology and instrumentation from Xidian University, Shaanxi, China, in 2011. He is currently pursuing his PhD at the National Laboratory of Radar Signal Processing, Xidian University. His research interests include maneuvering target detection, parameter estimation, and time-frequency analysis.

Tao Su received his BS in information theory, MS degree in mobile communication, and PhD in signal and information processing from Xidian University, Xi'an, China, in 1990, 1993, and 1999, respectively. He is currently a professor at the National Laboratory of Radar Signal Processing, Xidian University. His research interests include high-speed real-time signal processing on radar, sonar and telecommunications, digital signal processing, parallel processing system design, and FPGA IP design.

Yanyan Li received her BS and MS degrees in industrial design and signal and information processing from Xidian University, Xi'an, China, in 2008 and 2011, respectively. She is currently pursuing her PhD at the National Laboratory of Radar Signal Processing, Xidian University. Her research interests include ISAR imaging, target detection, and target tracking.

Jibin Zheng received his BS degree in electronic information science and technology from Shandong Normal University, Shandong, China, in 2009, and PhD in signal and information processing from Xidian University in 2015. Since 2015, he has been on the faculty at National Laboratory of Radar Signal Processing at Xidian University. His research interests include target detection, synthetic aperture radar (SAR) and inverse SAR signal processing, cognitive radar, and time-frequency analysis.